**Title**

MAGPI: A framework for maximum likelihood MR phase imaging using multiple receive coils.

**Permalink**

**Journal**

**Authors**

Dagher, Joseph
Nael, Kambiz

**Publication Date**

**DOI**

Peer reviewed

# MAGPI: A Framework for Maximum Likelihood MR Phase Imaging Using Multiple Receive Coils

**Joseph Dagher**[*] and **Kambiz Nael**

Department of Medical Imaging, The University of Arizona, Tucson, AZ

## Abstract

**Purpose—**Combining MR phase images from multiple receive coils is a challenging problem, complicated by ambiguities introduced by phase wrapping, noise and the unknown phase-offset between the coils. Various techniques have been proposed to mitigate the effect of these ambiguities but most of the existing methods require additional reference scans and/or use ad-hoc post-processing techniques that do not guarantee any optimality.

**Theory and Methods—**Here, the phase estimation problem is formulated rigorously using a Maximum-Likelihood (ML) approach. The proposed framework jointly designs the acquisition-processing chain: the optimized pulse sequence is a single Multi-Echo Gradient Echo scan and the corresponding post-processing algorithm is a voxel-per-voxel ML estimator of the underlying tissue phase.

**Results—**Our proposed framework (MAGPI) achieves substantial improvements in the phase estimate, resulting in phase SNR gains by up to an order of magnitude compared to existing methods.

**Conclusion—**The advantages of MAGPI are: (1) ML-optimal combination of phase data from multiple receive coils, without a reference scan; (2) ML-optimal estimation of the underlying tissue phase, without the need for spatial processing; and (3) robust dynamic estimation of channel-dependent phase-offsets.

### Keywords

MR Phase; Frequency Offset; Coil Array; Phase Offset; Maximum Likelihood

## INTRODUCTION

Quantitation using the magnitude of the reconstructed MR image is the predominant practice in various clinical applications. Recently, the phase of the MR signal has demonstrated its promise in expanding the quantitative capability of MRI. For example, the phase signal has been directly linked with Electro-Magnetic (EM) properties of tissues (such as susceptibility and conductivity), tissue temperature, venous oxygenation, blood velocity, tissue elasticity, among others (1, 2, 3, 4, 5, 6). The MR phase has also been extensively used for "fieldmap estimation" in the neuroimaging community to calculate and correct for the inhomogeneity

[*]Corresponding author: jdagher@email.arizona.edu; 1609 N. Warren Bldg 211 Rm 110, Tucson, AZ, USA, 85724; (520) 621-0809..

of the static field, $B_0$ (7, 8, 9, 10, 11). We note that, while $B_0$ is usually used to describe slowly spatially-varying field profile (8, 10), we use hereafter the term MR phase to indicate general voxel-per-voxel variations in the phase domain that would additionally be explained by inherent tissue properties (velocity, susceptibility, etc.)

While currently utilized MR pulse sequences and algorithms are optimized for magnitude-domain contrast or SNR, there are fundamental challenges that make SNR-optimal MR phase acquisition and estimation more difficult than magnitude.

### Phase noise and wrapping

We have shown in (7) that there are three phase-imaging regimes that acquisition methods operate in: (I) a regime dominated by phase-wrapping, with reduced levels of noise, (II) a regime dominated by noise, with minimal instances of phase-wrapping and (III) a regime where the original signal needs to be disambiguated from both phase-wrapping and noise contributions. It is not always possible to choose which regime to operate in due to hardware constraints (minimum echo time spacing, gradient strengths, bandwidth) or total imaging time restrictions.

Most single-echo acquisition methods operate in Regime III where post-processing is relied on in order to recover phase wrapping and noise errors. As rigorously documented in (12), phase unwrapping methods are not robust in the presence of noise, are computationally expensive and often require expert-user intervention. The authors in (12) have also shown that phase unwrapping is inefficient in the presence of moderately complex geometrical patterns. Furthermore, in order to mitigate the effects of noise, most single-echo phase processing methods rely on aggressive spatial averaging, such as 5×5×5 median filters (12). The impact of such a simplistic approach on phase quantitation could be detrimental and limits the spatial resolution of the resulting estimates.

Multi-echo acquisition methods, such as two-echo methods (9), three-echo methods (8, 12, 13) and higher (11, 14), are constrained to choose at least one of the echo step sizes to be small enough to avoid phase wrapping (Regime II). A shortcoming with these methods is the referencing of the phase amongst echoes (phase difference), which amplifies the noise even further. Hybrid methods use short echo steps to unwrap longer echo steps (8, 12, 13, 14) but, as we have shown in (7), such an approach results in error propagation. Our proposed solution in (7) was also based on phase difference, however, we chose 2 echo step sizes large enough (Regime I) to improve the noise performance and purposefully induce phase-wrapping. The wrapping pattern was precisely engineered in (7) such that a corresponding voxel-per-voxel estimation heuristic could disambiguate the original phase value.

### Phase-Offset

The phase-offset $\phi_{0,c}(x, y)$ varies both spatially and across the channels, due to dependence on coil position, cable lengths, and electronic delay (12). $\phi_{0,c}(x, y)$ also varies with time due to drifts in frequency synthesizer and/or imperfections in the centering of k-space (15). Combining coils' complex data is thus a challenging problem where existing solutions could be classified into methods that:

**(A)** invert the sensitivity profiles using SNR-optimal methods for multi-channel combination. However, this requires exact knowledge of the complex coil sensitivities (16) or data correlation matrices (17). To that end, popular methods utilize an additional reference scan to estimate $\phi_{0,c}(x, y)$, which assumes it to be temporally invariant over scan duration (18). Other methods approximate relative estimates of $\phi_{0,c}(x, y)$ from the acquired complex images (19). Severe artifacts and loss of phase information occur in areas where a good SNR is not maintained every pixel across more than one coil. This "virtual coil" approach also assumes slowly varying $\phi_{0,c}(x, y)$ across coils, and slowly varying tissue-phase across space (19).

**(B)** reference the measurements to either (i) a time point, (ii) a defined region of interest, or (iii) a coil. (i) Echo time referencing suffers from inherent SNR penalty due to noise amplification (18, 20). (ii) Referencing the phase signal to a user-defined region aligns the phase of the complex data in that region, but introduces artifacts and signal loss away from the reference region (21). (iii) Coil referencing requires a coil with good sensitivity across the entire FOV of interest.

## Our contribution

In this paper, we present a novel framework for MR phase imaging that jointly addresses the challenges outlined above. We formulate the phase estimation problem in rigorous terms and show that our reconstructed phase image is the Maximum-Likelihood (ML) estimate of the underlying tissue phase. Our framework does not require a reference scan, and does not increase the acquisition time. Furthermore, our reconstruction algorithm does not require the use of ad-hoc phase unwrapping/denoising methods, and is strictly a voxel-per-voxel approach, thus preserving the spatial resolution of the image.

We should note that another ML method has been proposed in the past for fieldmap estimation (8). As mentioned above, the work in (8) uses echo-referencing (phase difference) and a small echo step size in order to avoid phase wrapping and phase-offset ambiguities. The performance of the method in (8) is thus constrained by these ambiguities. Our approach, however, is fundamentally different: phase wrapping, phase-offset and phase noise ambiguities are all purposefully designed into the acquisition process. This novel framework enables a range of advantages not achievable with other methods, as we detail in the Discussion section.

## THEORY

We will consider here the theory associated with MR phase originating as a response to a Gradient-Echo (GRE) sequence. Similar analysis could be extended to other sequences. The measurement obtained using a GRE at channel (receiver) element $c$ and echo time $TE_k$ could be written as (22)

$$\mathbf{m}_{k,c}(x, y) = \rho_{k,c}(x, y)\, exp\left\{i\left(\phi_{0,c}(x, y) + 2\pi\Delta B(x, y)\, TE_k\right)\right\} + \mathbf{w}(x, y), \quad \text{[1]}$$

where the magnitude term $\rho_{k,c}(x, y)$ is the spin density at echo time $TE_k$ modulated by the sensitivity of channel $c$, $2\pi$ $B(x, y)TE_k$ is the underlying "tissue phase" value and $\phi_{0,c}(x, y)$ is the spatially-varying channel-dependent phase offset of channel $c$. Note that we use a left-hand coordinate system here to match the phase sign in our vendor's (Siemens) phase reconstructions. The tissue frequency term $B(x, y)$ accounts for all deviations in the main magnetic field at location $(x, y)$ due to the presence of the object. These deviations are due to both, inherent tissue properties (such local magnetic susceptibility changes), as well as object coil-loading effects. The noise term $\mathbf{w}(x, y)$ in each voxel is drawn i.i.d. from a complex Gaussian random variable, i.e. $\mathbf{w} = \mathbf{w}_R + i\mathbf{w}_I$, $\mathbf{w}_R$, $\mathbf{w}_I \sim \mathcal{N}(0, \sigma_w)$.

The goal of quantitation from MR phase is to extract the term $B(x, y)$ from the measurements $\mathrm{m}_{k,c}(x, y)$. Instead of the phase, however, we are restricted to the numerically computed angle of $\mathrm{m}_{k,c}(x, y)$, namely,

$$\Psi_{k,c}(x,y) = \phi_{0,c}(x,y) + 2\pi\Delta B(x,y)TE_k + \Omega_{k,c}(x,y) + 2\pi\mathbf{r}_{k,c}(x,y), \quad [2]$$

where $\Omega_{k,c}(x, y)$ is the phase contribution of the additive noise term and $\mathbf{r}_{k,c}(x, y)$ is a phase wrapping integer which forces the sum in [2] to be in the range $[-\pi, \pi)$. Therefore, the integer $\mathrm{r}_{k,c}(x, y)$ is a function of both echo time index $k$ and channel index $c$. Note that $\Omega_{k,c}(x, y)$ also depends on echo time and channel index. That is because the contribution of the noise $\mathbf{w}(x, y)$ to the phase depends on $\rho_{k,c}(x, y)$ (7).

Hereafter, we drop the pixel subscripts $(x, y)$ with the understanding that the remaining analysis applies separately to each voxel in the image.

### Maximum Likelihood Phase Estimation

Formally, the ML estimate of a parameter of interest $\theta$ from measurements g is obtained through maximizing the probability of obtaining g, given an underlying parameter model, namely:

$$\hat{\theta}_{ML} = \arg\max_{\theta} \mathrm{pr}(g/\theta) \quad [3]$$

where the conditional probability $\mathrm{Pr}(g/\theta)$ is the likelihood function. The popularity of ML estimation (MLE) is mainly due to its optimality properties such as efficiency, sufficiency, consistency and invariance (23). Other common estimators (e.g., Least Squares) do not possess such important properties. The Invariance property is very important in our view. Stated formally, if $\theta$ is the true value of a parameter and $\Theta = f(\theta)$ is a function of that parameter, then the ML estimate of $\Theta$ is given by:

$$\hat{\Theta}_{ML} = f\left(\hat{\theta}_{ML}\right). \quad [4]$$

That is, the ML estimate of a function of a parameter is the function of its ML estimate (23, 24). This property is key because the end goal is to extract paramaters from $B$.

In this problem, we are concerned with the estimation of parameter $B$ from $\psi_{k,c}$. We can show that the corresponding likelihood function, $\mathscr{L}_{k,c}$, is given by:

$$\mathscr{L}_{k,c}(\Delta B) \triangleq pr\left(\mathbf{\Psi}_{k,c}{=}\psi_{k,c}/\Delta B\right) {=} pr\left(\mathbf{\Omega}_{k,c}{+}2\pi\mathbf{r}_{k,c}{=}\psi_{k,c}-2\pi\Delta BTE_k-\phi_{0,c}\right) \quad [5]$$

where $\psi_{k,c}$ is a realization of the angle random variable $\mathbf{\Psi}_{k,c}$. Note that, because the phase wrapping integer $\mathbf{r}_{k,c}$ depends on the phase noise random variable $\mathbf{\Omega}_{k,c}$, this implies that $\mathbf{r}_{k,c}$ is also a (discrete) random variable. Using the total probability theorem, we can write:

$$\mathscr{L}_{k,c}(\Delta B) {=} \sum_r P\left(\mathbf{r}_{k,c}{=}r\right) f_{\mathbf{\Omega}_{k,c}}\left(\psi_{k,c}-2\pi\Delta BTE_k-2\pi r-\phi_{0,c}\right) \quad [6]$$

where $P\left(\mathbf{r}_{k,c}=r\right)$ is the probability of obtaining a given wrapping integer $r$ and $f_{\mathbf{\Omega}_{k,c}}$ is the Probability Density Function of the noise in channel c, at echo time k. We have derived both of these probabilities in closed form, with the wrapping probability given by (see Appendix A):

$$P\left(\mathbf{r}_{k,c}{=}r\right){=}\frac{\sigma_{k,c}\sqrt{2}}{4\Delta B_{max}}\left[\frac{e^{-b_2^2}-e^{-a_2^2}}{\sqrt{\pi}}-a_2 erf\left(a_2\right)+b_2 erf\left(b_2\right)-\frac{e^{-b_1^2}-e^{-a_1^2}}{\sqrt{\pi}}+a_1 erf\left(a_1\right)-b_1 erf\left(b_1\right)\right], \quad [7]$$

where, $\quad a_1{=}\dfrac{\left(\frac{2r-1}{2TE_k}-\Delta B_{max}\right)}{\sqrt{2}\sigma_{k,c}}, b_1{=}\dfrac{\left(\frac{2r+1}{2TE_k}-\Delta B_{max}\right)}{\sqrt{2}\sigma_{k,c}}, a_2{=}\dfrac{\left(\frac{2r-1}{2TE_k}+\Delta B_{max}\right)}{\sqrt{2}\sigma_{k,c}}, b_2{=}\dfrac{\left(\frac{2r+1}{2TE_k}+\Delta B_{max}\right)}{\sqrt{2}\sigma_{k,c}}, \quad [8]$

where $\sigma_{k,c}$ is the standard deviation of phase noise given by [25] (Appendix A). The phase noise distribution could also be derived in closed-form (see (7)):

$$f_{\mathbf{\Omega}_{k,c}}(\Omega){=}\frac{exp\left(-snr_{k,c}^2/2\right)}{2\pi}\left\{1{+}snr_{k,c}\sqrt{\frac{\pi}{2}}cos\Omega\,exp\left(snr_{k,c}^2 cos^2\Omega/2\right)\left[1{+}erf\left(\frac{snr_{k,c}\,cos\Omega}{\sqrt{2}}\right)\right]\right\} \quad [9]$$

where $\quad snr_{k,c}{=}0.65\,SNR_{0,c}\,e^{-\frac{TE_k}{T2^*}} \quad [10]$

and $SNR_{0,c}$ is the magnitude-domain SNR in channel c at TE= 0. We validate these derivations in Figure 1 where we plot the likelihood function using theoretical derivations (solid red line) and numerical simulations (blue cross markers), for various example voxels, $SNR_{0,c}$ and T2* values. We note the strong match between our theoretical predictions and the numerical simulations.

We focus here on the dependence of the likelihood functions on $TE_k$, $B$, T2* and $SNR_{0,c}$. We plot in Figure 2a two families of likelihood functions obtained in an example voxel at two different values of $TE_k$. We ignore the channel offsets ($\phi_{0,c} = 0$, $\forall c$) in this figure. Note first that, for long $TE_k$, the likelihood functions exhibit sharp but multiple global maxima, whereas short $TE_k$ yield a broad unimodal maximum. Second, we see that repeated measurements yield randomly shifted likelihoods (dashed family of lines of same color). Measurements at the longer $TE_k$ result in a family of likelihood functions that are more tightly distributed, as compared to the shorter $TE_k$. Both of these observations show that the likelihood function are subject to the inherent trade-offs with respect to the choice of $TE_k$: long $TE_k$ induce wrapping-dominated errors, while shorter $TE_k$ induce noise-dominated

errors. We include the effects of the unknown phase offset in Figure 2b, where we plot example $\mathscr{L}_{k,c}(\Delta B)$ for different channels. Note that likelihoods in the same voxel are now shifted with respect to one another by an unknown amount, $\phi_{0,c}$.

This example illustrates that maximizing the tissue frequency (or phase) likelihood is made difficult by: (1) a tradeoff between multiple global maxima or, a maximum whose location is sensitive to noise and (2) the unknown $\phi_{0,c}$. We propose next a framework which overcomes these fundamental challenges.

## Proposed Solution: MAGPI

Our proposed framework, coined MAGPI (Maximum AmbiGuity distance for Phase Imaging), acquires Multi-Echo Gradient Echo (MEGE) measurements from a collection of 3 echoes, and $N_c$ channels, within a single TR. The estimation step is described using the 3-pass process detailed below.

• **Pass I:** *Find the most likely* $\Delta B$ *that explains the angle buildup between echoes*—Instead of searching for the most likely tissue frequency value $\Delta B$ that explains the angle measurements of a given echo/channel $\psi_{k,c}$, we look for the most likely value that explains the *phase buildup* (i.e., phase difference) between echo pairs. Formally, we can show that the angle difference between two echoes $k = 1$ and $k = 2$ is:

$$\mathbf{\Delta\Psi_{2:1,c}} \triangleq \angle\left\{\mathbf{m_{2,c}m_{1,c}^*}\right\} = 2\pi\mathbf{\Delta B\Delta TE_{2:1}} + \mathbf{\Delta\Omega_{2:1,c}} + 2\pi\mathbf{r_{2:1,c}}, \quad [11]$$

where $\Delta TE_{2:1} \triangleq TE_2 - TE_1$, $\Delta\Omega_{2:1,c} \triangleq \Omega_{2,c} - \Omega_{1,c}$, and $\mathbf{r}_{2:1,c}$ is a phase wrapping integer which forces the sum in [11] to be in the range $[-\pi, \pi)$. There are two differences in [11] as compared to [2]. First, the measured angle buildup does not depend on $\phi_{0,c}$. The second difference is a reduced phase SNR (due to multiplication with a smaller term, $\Delta TE_{2:1}$, and noise amplification from two noise RVs instead of one). We will address this shortcoming in Pass III below. The dual-echo likelihood function, denoted by $\mathscr{L}_{2:1,c}(\Delta B) \triangleq pr(\Delta\Psi_{2:1,c}/\Delta B)$, is now given by:

$$\mathscr{L}_{2:1,c}(\Delta B) = \sum_r P(\mathbf{r}_{2:1,c}=r) f_{\mathbf{\Delta\Omega_{2:1,c}}}(\Delta\psi_{2:1,c} - 2\pi\Delta B\Delta TE_{2:1} - 2\pi r) \quad [12]$$

where the noise and wrapping probabilities $f_{\Omega_{2:1,c}}$ and $P(\mathbf{r}_{2:1,c})$ could be readily obtained in closed-form, similar to the derivations in [7] and [9]. Note that, in the absence of phase-offset ambiguity, the ML solution for each coil also maximizes the product of the dual-echo likelihoods over all coils, $\Pi_c\mathscr{L}_{2:1,c}(\Delta B)$. This product assumes that the angle measurements over all the coils are conditionally independent. This assumption may not be exact, due to noise correlation across coils, but we ignore any inter-coil dependence for now.

Nevertheless, dual-echo likelihoods still face here the same unimodal vs multimodal tradeoff as single-echo likelihoods. We address this limitation with the use of a third echo, $k = 3$, and we pose this question: what is the $\Delta B$ that most-likely explains *both* angle buildups from echo pairs {1,2} and {1,3}? Formally,

$$\widehat{\Delta B}_{(\mathrm{I})} = \underset{\Delta B}{argmax} \mathscr{L}_{\mathrm{I}}(\Delta B) \quad [13]$$

$$\text{where} \qquad \mathscr{L}_{\mathrm{I}}(\Delta B) = \prod_{k=2,3} \prod_{c} \mathscr{L}_{k:1,c}(\Delta B). \quad [14]$$

We make the following comments about [13]:

i.  We define $\mathscr{L}_1(\Delta B)$ as the "system likelihood." We claim that $\mathscr{L}_1(\Delta B)$ is not subject to the single noisy maximum vs multiple globale maxima tradeoff of single and dual echo likelihoods. Specifically, the logical argument we *disprove* here is: system likelihoods *always* possess multiple global maxima whenever the function is multimodal. We disprove this argument in Figure 3 using multiple counter-examples where $\mathscr{L}_1(\Delta B)$ is multimodal but has a single sharp global maximum. This was achieved despite the underlying dual-echo likelihoods possessing multiple global maxima (Figure 3a) or both unimodal and multimodal maxima (Figure 3b).

ii. The quality of the solution obtained from [13] depends on the choice of system likelihoods. For example, in the ideal limit of infinite SNR, we can show that it is possible to achieve a system likelihood equal to a Dirac delta function, perfectly positioned at the true $B$. Any deviation from this ideal system likelihood function inevitably yields loss of estimation performance.

iii. For a given $B$, T2* and $\mathrm{SNR}_{0,c}$ in a voxel, it is obvious that there exists a large number of system likelihood functions (selected by $\mathrm{TE}_k$) that one could choose from. Bullet i and ii above point to the fundamental key to our method: the design of acquisition parameters (echo times) such as the resulting system likelihood is as close as possible to the ideal system likelihood function. We develop this idea more fully in the Optimizer section below.

The estimation problem could be terminated at this step but, the performance at this stage is limited by the inherent noise amplification through the use of the product in [11]. We address this issue in the two following steps.

• **Pass II:** *Estimate the channel-dependent phase offsets $\varphi_{0,c}$*—After obtaining an ML estimate of $B$ in Pass I, the *remaining* data in the original measurements [2] that is unexplained by the Pass I model [11] can be attributed to $\varphi_{0,c}$ and errors in the $B$ estimate.

The task in this step is to extract $\varphi_{0,c}$ from these remainder terms: $\phi_{k,c}^{rem} = \angle\left(\mathrm{m}_{k,c} e^{-i\widehat{\Delta B}_{(\mathrm{I})}}\right)$. To achieve this, we take advantage of the following distinct features of $\varphi_{0,c}$: smooth variation over space and invariance with echo times. Using this prior knowledge, we can use various signal-separation techniques to extract $\varphi_{0,c}$ from $\phi_{k,c}^{rem}$. We resort here to a simple spatio-temporal low-pass filter applied in the Fourier domain $\hat{\phi}_{0,c} = \mathscr{LPF}\left\{\phi_{k,c}^{rem}\right\}$ (12).

- **Pass III**: *Find the most likely $B$ that explains the angle of the three echoes—*

After obtaining the estimate of $e^{i\varphi_{0,c}}$ from Pass II, we can rewrite the single-echo likelihood functions in [6] without any channel-offset ambiguity, namely:

$$\mathscr{L}_{k,c}\left(\Delta B\right) \underline{\underline{\Delta}} pr\left(\mathbf{\Psi}'_{k,c}=\psi'_{k,c}/\Delta B\right)=\sum_{r}P\left(\mathbf{r}_{k,c}=r\right)f_{\mathbf{\Omega}_{k,c}}\left(\psi'_{k,c}-2\pi\Delta B TE_k-2\pi r\right) \quad [15]$$

$$\text{where}\qquad \psi'_{k,c}=\angle m_{k,c}e^{-i\phi_{0,c}}. \quad [16]$$

Thus, in this pass, we ask the following MLE question: what is the most likely tissue frequency that could explain the angles, as given by [16]? We can answer this question here without resorting to phase differencing. Formally, we solve:

$$\widehat{\Delta B}_{(III)}=\underset{\Delta B}{argmax}\,\mathscr{L}_{III}\left(\Delta B\right) \quad [17]$$

$$\text{where}\qquad \mathscr{L}_{III}\left(\Delta B\right)=\prod_{k=1}^{3}\prod_{c}\mathscr{L}_{k,c}\left(\Delta B\right). \quad [18]$$

$\mathscr{L}_{III}\left(\Delta B\right)$ is another system likelihood, given by the product of the three individual likelihoods, over all channels. We make the same notes about the system likelihoods of Pass III as those of Pass I: (i) the system likelihoods are not subject to the noise-wrapping trade-offs of individual likelihoods, and (ii) we advocate the design of $\mathscr{L}_{III}$ (through selection of $TE_k$) to be as similar to a Dirac delta as possible.

We emphasize that the main goal of Pass I in our algorithm is to create a "rough unbiased estimate" of $B$, so that Pass II could remove it from the original data and create a residue image $\phi^{rem}_{k,c}$. This residue image is then used in Pass II to separate random noise fluctuations from phase-offsets $\phi_{0,c}$. Once phase-offsets are computed, Pass III revisits the $B$ estimation step, this time without the need for echo referencing (or phase differences). As we will show in our results, there is no error propagation from Pass I to Pass III.

## MAGPI Optimizer

The solutions to problems [13] and [17] are not guaranteed to yield the "best" tissue frequency (and tissue phase) estimate for arbitrary choices of echo times. As mentioned in Pass I and Pass III, a careful optimization routine picks the echo times such that the resulting likelihoods, $\mathscr{L}_{I}\left(\Delta B\right)$ and $\mathscr{L}_{III}\left(\Delta B\right)$, are as close to Dirac delta functions. Denote by $\mathscr{D}\left(f\left(\Delta B\right),\delta\left(\Delta B\right)\right)$, a distance measure between an arbitrary function $f$ and the Dirac delta function centered at $B$. Ideally, we would want to minimize both $\mathscr{D}\left(\mathscr{L}_{I}\left(\Delta B\right),\delta\left(\Delta B\right)\right)$ and $\mathscr{D}\left(\mathscr{L}_{III}\left(\Delta B\right),\delta\left(\Delta B\right)\right)$, for all possible values of $B$ and measurements. There are various ways to approach this challenging multiobjective optimization problem. In this work, we propose to minimize the average $\mathscr{D}\left(\mathscr{L}_{III}\left(\Delta B\right),\delta\left(\Delta B\right)\right)$ subject to upper bound constraints on the average $\mathscr{D}\left(\mathscr{L}_{I}\left(\Delta B\right),\delta\left(\Delta B\right)\right)$. The motivation for this choice is that the $B$ estimate from Pass III is the final estimate, and thus should be optimally chosen. The $B$

estimate from Pass I, however, needs to be constrained so that its errors to Pass II are only limited by unbiased random noise (and not biased by phase wrapping). Formally, the optimization problem is as follows:

$$\left[TE_1^{opt}, TE_2^{opt}, TE_3^{opt}\right] = \underset{[TE_1,TE_2,TE_3]}{arg\,min} \; \mathbb{E}[\mathscr{D}(\mathscr{L}_{III}(\Delta B), \delta(\Delta B))]_{\Omega_k, r_k, \Delta B}$$
$$such\;\;that,\;\;\;\;\mathbb{E}[\mathscr{D}(\mathscr{L}_I(\Delta B), \delta(\Delta B))]_{\Omega_k, r_k, \Delta B} <= \epsilon_I \;\;\; \& \;\;\; [TE_1, TE_2, TE_3] \in \mathscr{C}_{TE}, \tag{19}$$

where $\mathscr{C}_{TE}$ is the set of allowable echo times, which takes into account constraints such as the minimum echo time spacing ( $TE_{min}$) and the minimum echo time ($TE_{min}$) achievable with the pulse sequence of choice. We note the following:

i.   *Distance measures*. There is a large variety of distance measures $\mathscr{D}(f(\Delta B), \delta(\Delta B))$. In this work, we use the Kullback-Leibler distance measure as the statistical distance between the distributions (23, 24). Other distance measures could be proposed.

ii.  *Design Specifications*. We emphasize that it is the pulse sequence of choice that defines the optimization design specifications. These specifications include constraints on echo timings such as ($TE_{min}$, $TE_{max}$ and $TE_{min}$). Also, since $SNR_{0,c}$ and T2* are spatially-varying quantities, we only optimize the echoes over the minimum $SNR_{0,c}$ and T2* of interest, $SNR_{0,min}$ and $T2^*_{min}$, as expected with the pulse sequence of choice. Voxels with SNRs larger than $SNR_{0,min}$ are guaranteed to never do worse than this worst-case voxel.

iii. *Tissue Frequency Prior information*. We assume in [19] a uniform distribution for $B$ within $\pm B_{max}$, which could be readily approximated based on the strength of the B0 field and the anatomy of interest.

iv.  *Computation*. Since the optimizer is run offline, once, various design specifications (see above) corresponding to different sequences of interest could be tabulated and used at acquisition time. Because of the closed form of the probability distributions of noise and phase wrapping, we can use Monte Carlo methods to rapidly compute the expectation in [19]. We solve the optimization problem using Genetic Optimization methods. The optimization step takes anywhere between 1-5 minutes on a personal computer, depending on the size of the constraint set $\mathscr{C}_{TE}$.

## METHODS

### ML-MAGPI Phase Reconstruction

We applied our 3-pass ML MAGPI algorithm outlined above. The reconstruction method in either Pass I or Pass III follows these steps independently in each voxel:

1.   The likelihood functions ([12] and [15]) are estimated at each echo time and channel.

i.   The SNR in each voxel, channel and echo time is approximated by computing the ratio of the magnitude signal to the noise standard deviation in the background region. This ratio approximates $snr_{k,c}$ in [10] which

allows rapid computation of the noise probability distribution [9], phase noise standard deviation [25] and phase wrapping probability distribution [7].

2. The system likelihoods are computed in Pass I and Pass III, by taking the product of the likelihoods functions computed in the step above, according to [13] and [17], respectively.

3. The system likelihoods are maximized. Although the system likelihoods could possess local maxima, the global maximum can be obtained rapidly with "brute force" search methods since the likelihoods are given by a 1-dimensional analytical expression.

4. Given that the likelihood are guaranteed to have a single global maximum in the optimization step (see Optimizer), the search method is guaranteed to return one single solution.

We performed these computations *serially* on a personal computer (Mac Pro, dual 3.1GHz CPU, 8 core each) using code written in MATLAB. Reconstructing a $256 \times 256$ B map, after running all three passes, took around 2 minutes. These rapid computations can be further accelerated using the highly parallelizable nature of the voxel-per-voxel approach. Unless otherwise noted, all of the MAGPI B estimates presented below are those obtained at Pass III.

### Literature Methods

We compared to the following methods from the literature throughout our experiments below:

i. Phase Difference (PD): This popular method uses a dual-echo approach to combine and estimate B maps (20).

ii. Single Echo + Reference: This method is based on a single-echo acquisition along with a separate reference scan (18). The combined phase is subsequently unwrapped and denoised, using standard techniques (18).

iii. UMPIRE: This triple-echo MEGE method was shown in (12) to outperform phase unwrapping algorithms in estimating tissue phase with complex geometries. The UMPIRE echoes are chosen here according to the prescription in (12), whereby the smallest difference between two echo steps is able to unwrap a maximum tissue frequency buildup of ±125Hz according to the constraints imposed by the utilized 3D sequence. In order to maintain the same spatial resolution across all methods, we did not employ any spatial denoising with UMPIRE.

iv. Adaptive Combine: This single-echo Siemens product sequence inverts the sensitivity profile of the coil array using SNR-optimal methods described in (17). This requires the use of a reference scan.

v. Homodyne-Processed Phase: This popular method (3) first high-pass filters the complex data (to reduce the contributions from phase-offsets), then the result is

coherently added. Clearly, the filtering results in loss of information from the underlying tissue phase of interest.

## Simulations

We validated the performance of our proposed MAGPI framework on a modified Shepp-Logan phantom using a $128 \times 128$ tissue frequency map, and a corresponding magnitude image with a homogeneous T2* of 40ms. We simulated a GRE acquisition of this complex-domain object using an array of 16-channel receive coils (25) at different SNRs. We evaluated the performance of our proposed method in reconstructing the tissue frequency map, and compared to some of the literature methods above.

## Phantom Study

We also validated the performance of MAGPI in phantom studies. A water phantom was acquired at 1.5T on a Siemens Aera scanner using a 20-channel head coil. Figure 6a shows an example magnitude combined (SSQ) image of the phantom at a short echo time. We computed the frequency map using the following 3D GRE-based methods:

**i.** <u>$20\times$ Averaged PD</u> with $TE_1 = 3.52$ms and $TE_2 = 9.38$ms, 20 averages each, TR = 20ms. This serves as the reference we compare our results to.

**ii.** <u>Single Echo + Reference</u> at TE = 40ms, TR = 45ms, with TA = 5min30s for both scans. We use the channel-dependent phase-offsets estimated from the $20\times$ Averaged PD scan above as the reference scan.

**iii.** <u>UMPIRE</u> at TE = {6.67, 21.67, 40}ms, TR = 45ms, TA = 3min09s.

**iv.** <u>MAGPI</u> at echo times TE = {16.01, 27.51, 34.87}ms, TR = 40ms, TA = 2min45s. These echoes were optimized for a $T2^*_{min}$ of 40ms, $SNR_{0,min} = 28$dB, and $B_{max} = 125$Hz. The MEGE sequence constraints were $TE_{min} = 5.82$ms and $TE_{min} = 6.1$ms.

The following were the common pulse-sequence parameters used by all methods above: 3D GRE, FOV = 220(read out) $\times$ 200mm$^2$, $N_x = 256$, $N_y = 232$, slice thickness 0.9mm, FA = 15°, BW=240Hz/pxl. The voxel size in this scan is thus $0.9 \times 0.9 \times 0.9$ mm$^3$.

## *in Vivo* Study

The brain of healthy volunteers was imaged after approval was obtained from our Institutional Review Board (IRB) and informed consent was given by the subjects. All scans were done on a Siemens Aera 1.5T with a 20-channel head coil. We acquired three types of scans: (Scan SR) standard-resolution mode, (Scan HR) high-resolution mode, and (Scan HT) standard-resolution mode with half the TR, i.e. half the acquisition time. For each scan type, we collected data using standard single echo GRE sequences, where the phase map was generated using both, the Adaptive Combine technique and the "Homodyne-Processed Phase" method. We also collected these three scans using our MAGPI protocol. The echo times optimized by [19] used $T2^*_{min}=40ms$, $SNR_{0,min} = 28$dB and $B_{max} = 125$Hz (as expected at 1.5T in the brain). Details of the scans are shown in Table 1.

## RESULTS

### Numerical Phantom

We generated 1000s of different realizations of $B$ maps, random noise and phase-offset patterns in our numerical phantom. We plot in Figure 4a the RMSE of the reconstructed tissue frequency as a function of the underlying $SNR_0$ in the image (SNR at TE=0) for the following methods:

1. PD (*blue dashed lines*): two PD methods ((PD-40, × marker) and (PD-10, + marker)) use a 3.5ms echo step which avoids phase wrapping for frequencies within ±125Hz. The PD-40 method uses echoes at {36.5, 40}ms. The 40ms echo is chosen for its utility as a magnitude contrast, while the PD-10 method uses echoes at {6.5, 10}ms.

2. Single Echo + Reference (*green solid line with squares*) at TE= 40ms. Here, we assume *perfect* knowledge of the phase-offset maps. Thus, errors in this method are only due to wrapping and noise.

3. UMPIRE (*dash-dotted magenta line*) at TE= {6.67, 21.67, 40}ms.

4. MAGPI (*red solid line*) which used TE= {16.01, 27.51, 34.87}ms for $SNR_0 < 30$dB and TE= {26.56, 35, 40.91}ms for $SNR_0$ 30dB. The first set of echoes was optimized for $SNR_{0,min} = 30$dB, and the second set for $SNR_{0,min} = 27$dB, both with $T2^*_{min}=40ms$, and $B_{max} = 125$Hz.

5. 1-Echo-Limit (*solid black line with upside-down triangles*): This method assumes (a) perfect knowledge of $\phi_{0,c}$ and (b) $B$ values that induce no phase wrapping. Thus, the only errors with this method would be due to noise. This constitutes a lower bound on the RMSE obtained with single echo scans.

6. ML bound (*solid black line with rightside-up triangles*): This is another theoretical lower-bound predicting the lowest RMSE achievable with ML-based methods with 3 echoes. This bound was derived by numerically computing the Fisher-Information (discussion beyond scope here).

An example phantom and corresponding estimates obtained with PD-40, UMPIRE and MAGPI at $SNR_0 = 27$dB are shown in Figures 4c-f, respectively, with the corresponding RMSE shown in the sub-captions. An $SNR_0$ of 27dB, or 22.38 unitless, corresponds to an SNR of 8.23 at TE=40ms with our T2* of 40ms. In such a low SNR regime, we see that PD-40 and UMPIRE are not robust, and exhibit noise-induced phase wrapping. MAGPI clearly outperforms both of these methods and is able to correctly recover both low and high $B$ values. In this example, MAGPI achieves RMSE reductions by a factor of 22.37 (over PD-40) and 30.13 (over UMPIRE). The resulting RMSE with MAGPI of 0.61Hz at such a low SNR is impressive. We also show in Figures 4g and 4h an example of the 16-channel phase-offsets used in the simulations and the corresponding estimate obtained using MAGPI at an SNR of 27dB, respectively.

### Real Phantom

Figure 5 shows the resulting frequency maps obtained in the phantom for each of the PD-10 (Figure 5a), Single-Echo + Reference (Figure 5b), UMPIRE (Figure 5c) and MAGPI (Figure 5d). Figure 6b shows the 20-channel phase-offsets as estimated using the 20× averaged PD-10 method while Figure 6c shows the corresponding phase-offsets as estimated with MAGPI.

### in Vivo

Figure 7 shows the frequency maps obtained by each of the Adaptive Combine (first column) and MAGPI (second column) techniques, for Scans SR (row 1), HT (row 2) and HR (row 3).

The homodyne-combined frequency images are shown in Figure 8. The first column are the results obtained with the single-echo methods, for each of the scan types (across rows). The second column is the result of applying the exact same homodyne filter, as used with the first column, on the MAGPI frequency images of Figures 7b, 7d and 7f.

## DISCUSSION

We have presented a novel theory and corresponding method for combining MR phase images, acquired using a coil-array, in an ML-optimal sense. Our proposed optimizer designs the acquisition process, by engineering the System Likelihood for optimal phase SNR in reconstruction.

All our closed-form derivations of probability distributions and likelihood functions were validated through rigorous numerical simulations. We emphasize two observations from the theoretical treatment. First, contrary to common assumptions, the phase noise is inadequately represented by a Gaussian probability distribution (Figures 1b and 1c), particularly at low SNRs. Second, our derivations show that the probability of obtaining a given wrapping integer is not always uniform over all possible wrapping values ([7] and Figure 1a). This is due to noise-induced phase wrapping effects at the boundary of the range of $B$ values.

We have validated the optimality of our proposed framework using numerical phantoms (Figure 4). The results in Figure 4a show that MAGPI is able to accurately recover the tissue frequency estimate at all SNRs, while overcoming the trade-offs and limitations of other methods. For example, note that the single-echo Phase Unwrapping method (Phun w/ $\phi_0$) fails to correctly unwrap the tissue phase (despite its assumed ideal reference scan) for our moderately complex phantom geometry. This is consistent with results reported in (12). PD-40 and UMPIRE are not robust, as their performance quickly degrades in the presence of noise. PD-10 outperforms PD-40, as expected, due to its shorter echo times, albeit without the desired magnitude contrast of longer echoes. The lower bound on the RMSE of single-echo methods (line with inverted triangles) shows the expected noise-only trend in the absence of phase wrapping and phase-offset ambiguities. The performance gains (RMSE reductions) with MAGPI, shown in Figure 4b, are particularly significant at low SNRs. MAGPI achieves a gain of ~11× (at all SNRs) over PD-10. MAGPI's gains over UMPIRE

increases as SNR decreases, ranging from 3.83× at 40dB to 41× at 27dB. Furthermore, MAGPI outperforms even the lower bound for ideal single echo methods by a factor of 1.81× at 40dB up to 3.9× at 27dB.

We also show in Figure 4a the RMSE of MAGPI's Pass I only (red dotted line) and note that it is always larger than the RMSE of Pass III due to the inherent noise amplification of echo referencing (phase difference) methods. Thus, we strongly advocate running all 3 passes of the algorithm. Figure 4a also plots on the right axis (brown color) the bias in MAGPI's $B$ estimate as a function of SNR for both Pass I (circles) and Pass III (X). This plot asserts that MAGPI is an unbiased estimator of tissue frequency and phase. Finally, we note from this figure that MAGPI's RMSE in Pass III is very close to the Minimum Variance Unbiased (MVU) bound predicted by theory (line with right-side up triangles). This shows that our ML estimation algorithm is efficient. This observation also implies that the errors from Pass I do not propagate to Pass III. This is expected: recall that Pass II selects spatially smooth terms in the residue image from Pass I (channel offsets) and discards high spatial frequency terms. Since the errors in Pass I are only due to random noise fluctuations (no bias), Pass II will inhibit these errors from propagating to Pass III.

The real phantom results are consistent with the numerical simulations. As can be seen from Figures 5a-d, we note a similarity in the $B$ estimate amongst all methods, yet with a clear SNR improvement obtained with MAGPI. In order to quantify this SNR gain, we removed any smooth background phase variations in the phantom, and displayed the result in second row of Figure 5. Since this is a water-only phantom, the result of such filtering process is mainly due to noise inherent in the $B$ estimate. The reduced level of noise in MAGPI's estimate (Figure 5h) is clear. The reported reduction in noise standard deviation (or gain in phase SNR) with MAGPI was: 3.95× over the 20-time averaged PD-10, 3.661× over Single Echo+Reference and a 7.9× over UMPIRE. These gains are consistent with our predictions from simulations (Figure 4b at $SNR_0$ of 32dB in this water phantom) where the expected gains are: 12× over PD-10 (for 1 average, or 2.7× with 20 averages), 3.7× over ideal single-echo methods (such as the Single-Echo+Reference scan in a phantom which has no wrapping ambiguity) and 8.1× over UMPIRE. We emphasize here that the acquisition time with MAGPI was the shortest amongst all methods.

We point out the ring structure in the MAGPI image (Figure 5h). These rings, also visible in the phantom's windowed magnitude image (Figure 6a), are due to truncation artifacts in 3D. These rings are not discernible in other phase estimation methods, due to being buried within large noise variations. MAGPI is able to overcome these noise limits without spatial smoothing.

Similar SNR gains are also seen with our *in-vivo* experiments. Figure 7 shows that the Adaptive Combine method suffers from severe phase artifacts due to both, inaccurate phase-offset inversion and phase unwrapping errors. MAGPI, however, was able to reconstruct the underlying $B$ without any artifacts, for all three scan types. MAGPI's SNR advantage is best visualized in "homodyne" domain, as shown in Figure 8. The traditional single echo method achieves poor phase SNR, especially in Scans HT and HR. Scan HT is particularly challenging, due to its reduced SNR (short TR) and reduced phase accumulation (short TE).

The corresponding homodyne MAGPI images (second column), obtained using the same homodyne filter, show substantially improved phase SNR over the traditional homodyne method for every scan type. In Scan SR, the phase SNR gain with MAGPI is evident with improved resolution of fine cortical structures and basal ganglia (Figure 8a vs. 8b). The gain obtained with MAGPI is even higher for Scans HT and HR, which have lower $SNR_0$ than Scan SR. This is expected from simulations where we showed that the gain of MAGPI over single-echo methods increases as $SNR_0$ decreases. This gain is translated in Scans HT and HR into improved CNR and ability to identify deep brain structures such as basal ganglia in Figures 8e and 8h when compared to almost non-diagnostic Figures 8d and 8g, respectively. Note that the high-pass filters with MAGPI are applied directly on the estimated *B* maps, rather than in complex domain as is done with single-echo methods. This enables the use of specialized high-pass filters with MAGPI that are better suited at preserving edges with reduced artifacts and noise amplification. One such filter is the Bilateral filter (26), shown in the third column of Figure 8. The bilateral filter achieves similar contrast and SNR gains obtained with homodyne MAGPI, albeit with reduced artifacts (such as blooming and edge effects) especially around cortical regions. We draw attention in particular to Figure 8f and note its improved phase SNR and comparable contrast compared to the single-echo SR scan of Figure 8a despite requiring half the latter's acquisition time.

MAGPI's phase SNR gains in Scan HR are highlighted in Figure 9, where we show a *B* estimate combined over a stack of 4 slices (8mm slab), using both the traditional single echo homodyne method (Figure 9a) and MAGPI+Bilateral filtering (Figure 9b). Using our technique, we observe high resolution images at 1.5T resulting in diagnostic image quality with excellent SNR and CNR as compared to standard single echo methods where accentuated noise clearly impairs definition of fine structural details. We emphasize that the acquisition time with MAGPI in this scan was 15% shorter than the traditional single-echo scan, further highlighting the impact of the choice of MAGPI's echo times on the SNR of the phase image.

Finally, our proposed ML framework is fundamentally different than the ML fieldmap estimation method previously presented in (8). As shown above, our system likelihoods modulate the inherent phase ambiguities, whereas the likelihood function in (8) is constrained by phase wrapping and phase-offsets. The following are some practical results of this important difference:

**i.** The Funai method uses a phase difference method in order to (a) minimize phase wrapping errors and (b) cancel channel-dependent phase offsets. As we have shown here, such an echo referencing approach suffers from inherent noise amplification (Pass I vs Pass III).

**ii.** The Funai method requires the use of at least one short echo time step size in order to *avoid* phase wrapping. That further amplifies noise and introduces error propagation onto the long echo steps. MAGPI, on the other hand, engineers phase wrapping as part of the likelihood function to achieve a significant phase SNR advantage.

    **iii.** The work in Funai's paper requires the use of multiple GRE acquisitions in order to accommodate short echo step sizes. MAGPI cuts the acquisition time substantially by incorporating purposefully wrapped long echo times into one MEGE acquisition.

    **iv.** Unlike MAGPI's voxel-per-voxel approach, the Funai method requires spatial regularization. This introduces bias, and increases computation cost, as noted by Funai *et.al*.

## CONCLUSION

We proposed here a novel framework which enables the design of phase-SNR optimal sequences. The overall advantages of our framework are the following: (1) ML-optimal combination of phase data from multiple receive coils, without a reference scan; (2) ML-optimal estimation of the underlying tissue phase, without the need for spatial averaging, denoising or phase unwrapping; and (3) dynamic estimation of channel-dependent phase-offsets. The result is an achieved gain in the phase image SNR by up to an order of magnitude compared to existing methods. In particular, the gain over ideal single-echo methods, which are free of wrapping and phase-offset errors, is at least a factor of $3.7\times$ at low SNRs. We have used such gains here to enable higher resolution, higher CNR, and more rapid phase imaging at 1.5T.

## ACKNOWLEDGMENTS

## APPENDIX A

We derive here the probability distribution of the phase wrap integer $\mathbf{r}_{k,c}$. We assume here that $\varphi_{0,c} = 0$, since the channel offsets are generally canceled out in Passes I and III. The analysis could be easily extended to non-zero channel offsets. From (2) we know that $\mathbf{r}_{k,c} = 0$ if the sum of $2\pi \ B\mathrm{TE}_k + \Omega_{k,c}$ is always within $[-\pi, +\pi]$. Or, in general, we can write:

$$Pr\left(\mathbf{r}_{k,c}{=}r\right) = \ \ Pr\left(-\pi + 2\pi r \leq 2\pi\Delta B\mathrm{TE}_k + \Omega_{k,c} \leq \pi + 2\pi r\right) \quad [20]$$

$$= \ \ Pr\left(-\frac{1}{2TE_k} + \frac{r}{TE_k} \leq \Delta B + \frac{\Omega_{k,c}}{2\pi TE_k} \leq \frac{1}{2TE_k} + \frac{r}{TE_k}\right) \quad [21]$$

$$= \ \ \int_{-\frac{1}{2TE_k}+\frac{r}{TE_k}}^{\frac{1}{2TE_k}+\frac{r}{TE_k}} \left(pr_{\Delta B} * f_{\phi_{k,c}}\right)(\zeta)\, d\zeta \quad [22]$$

$$= \frac{1}{2\Delta B_{max}} \int_{-\frac{1}{2TE_k}+\frac{r}{TE_k}}^{\frac{1}{2TE_k}+\frac{r}{TE_k}} d\zeta \int_{\zeta-\Delta B_{max}}^{\zeta+\Delta B_{max}} dt\, f_{\phi_{k,c}}(t) \quad [23]$$

$$\approx \frac{1}{4\Delta B_{max}} \int_{-\frac{1}{2TE_k}+\frac{r}{TE_k}}^{\frac{1}{2TE_k}+\frac{r}{TE_k}} d\zeta \left[ erf\left(\frac{\zeta+\Delta B_{max}}{\sigma_{k,c}\sqrt{2}}\right) - erf\left(\frac{\zeta-\Delta B_{max}}{\sigma_{k,c}\sqrt{2}}\right) \right] \quad [24]$$

where [22] uses the convolution theorem for the sum of 2 independent random variables, and [23] assumes $B$ to be uniformly distributed between $\pm B_{max}$. This assumption makes sense in the absence of prior information about tissue frequency. In these equations, $f_{\phi_{k,c}}(\zeta)$ is the probability distribution of the phase noise ($\phi_{k,c} = \Omega_{k,c}/2\pi TE_k$, units in Hz) given by a scaled version of [9]. In [24], we carry out the integral by approximating $f_{\phi_{k,c}}(\zeta)$ with a Gaussian with the same standard deviation $\sigma_{k,c}$. Finally, using known properties of integral of error functions the final form of the phase wrapping probability distribution in [7] follows.

We note here that $\sigma_{k,c}$ could also be derived in closed form, and is readily given by (27):

$$\sigma_{k,c}^2 = \frac{1}{4\pi^3 TE_k^2} exp\left(-\frac{1}{2}snr_{k,c}^2\right) \left[ \alpha_0 + \sum_{n=1}^{\infty} \frac{\alpha_n}{(2n-1)!!} snr_{k,c}^{2n} + \sqrt{\frac{2}{\pi}} \sum_{n=0}^{\infty} \frac{\beta_n}{(2n)!!} snr_{k,c}^{2n+1} \right] \quad [25]$$

where $snr_{k,c}$ is given by [10], and $\alpha_n$ and $\beta_n$ are closed form polynomials rapidly decaying with $n$ given by:

$$\alpha_n = \frac{2n-1}{2n}\alpha_{n-1} + \frac{2\pi}{(2n)^2}\left[1 - \frac{(2n-1)!!}{(2n)!!}\right], n=1, 2, \ldots \quad [26]$$

$$\beta_n = \frac{2n}{2n+1}\beta_{n-1} - \frac{2\pi}{(2n+1)^2}, \quad n=1, 2, \ldots \quad [27]$$

$$\alpha_0 = \frac{\pi^3}{3}, \beta_0 = -2\pi. \quad [28]$$

## REFERENCES

1. Schweser F, Deistung A, Lehr BW, Reichenbach JR. Quantitative imaging of intrinsic magnetic tissue properties using MRI signal phase: An approach to in vivo brain iron metabolism? NeuroImage. Feb; 2011 54(4):2789–2807. [PubMed: 21040794]

2. Schweser F, Sommer K, Deistung A, Reichenbach JR. Quantitative susceptibility mapping for investigating subtle susceptibility variations in the human brain. NeuroImage. Jun; 2012 62(3): 2083–100. [PubMed: 22659482]

3. Haacke, EM.; Reichenbach, JR. Susceptibility weighted imaging in MRI: basic concepts and clinical applications. Wiley-Blackwell; 2011.

4. Rieke V, Butts Pauly K. MR thermometry. Journal of Magnetic Resonance Imaging. 2008; 27(2): 376–390. [PubMed: 18219673]

5. Lotz J, Meier C, Leppert A, Galanski M. Cardiovascular flow measurement with Phase-Contrast MR imaging: Basic facts and implementation1. Radiographics. 2002; 22(3):651–671. [PubMed: 12006694]

6. Mariappan YK, Rossman PJ, Glaser KJ, Manduca A, Ehman RL. Magnetic resonance elastography with a phased-array acoustic driver system. Magnetic Resonance in Medicine. 2009; 61(3):678–85. [PubMed: 19132758]

7. Dagher J, Reese T, Bilgin A. High–resolution, large dynamic range field map estimation. Magnetic Resonance in Medicine. Jan; 2014 71(1):105–17. [PubMed: 23401245]

8. Funai A, Fessler J, Yeo D, Noll D. Regularized field map estimation in MRI. IEEE Transactions on Medical Imaging. 2008; 27(10):1484–1494. [PubMed: 18815100]

9. Jezzard P, Balaban R. Correction for Geometric Distortion in Echo Planar Images from B0 Field Variations. Magnetic Resonance In Medicine. Jul; 1995 34(1):65–73. [PubMed: 7674900]

10. Nguyen H, Sutton B, Morrison R Jr, Do M. Joint Estimation and Correction of Geometric Distortions for EPI functional MRI using Harmonic Retrieval. IEEE Transactions on Medical Imaging. 2009; 28(3):423–434. [PubMed: 19244014]

11. Chen N, Wyrwicz A. Correction for EPI distortions using multi-echo gradient-echo imaging. Magnetic Resonance In Medicine. 1999; 41(6):1206–1213. [PubMed: 10371453]

12. Robinson S, Schödl H, Trattnig S. A method for unwrapping highly wrapped multi-echo phase images at very high field: UMPIRE. Magnetic Resonance In Medicine. Jul; 2014 72(1):80–92. [PubMed: 23901001]

13. Aksit P, Derbyshire J, Prince J. Three-point method for fast and robust field mapping for EPI geometric distortion correction. 4th IEEE International Symposium on Biomedical Imaging. 2007:141–144.

14. Feng W, Neelavalli J, Haacke EM. Catalytic multiecho phase unwrapping scheme (CAMPUS) in multiecho gradient echo imaging: Removing phase wraps on a voxel-by-voxel basis. Magnetic Resonance In Medicine. 2013; 70(1):117–26. [PubMed: 22886762]

15. Huber KM, Roland J, Schoepfer J, Biber S, Martius S. Using MR thermometry for SAR verification in local pTX applications. International Society for Magnetic Resonance in Medicine. 2013; 21

16. Roemer PB, Edelstein WA, Hayes CE, Souza SP, Mueller OM. The NMR phased array. Magnetic Resonance In Medicine. Nov; 1990 16(2):192–225. [PubMed: 2266841]

17. Walsh DO, Gmitro AF, Marcellin MW. Adaptive reconstruction of phased array MR imagery. Magnetic Resonance In Medicine. May; 2000 43(5):682–690. [PubMed: 10800033]

18. Robinson S, Grabner G, Witoszynskyj S, Trattnig S. Combining phase images from multi-channel RF coils using 3D phase offset maps derived from a dual-echo scan. Magnetic Resonance In Medicine. Jan; 2011 65(6):1638–1648. [PubMed: 21254207]

19. Parker DL, Payne A, Todd N, Hadley JR. Phase reconstruction from multiple coil data using a virtual reference coil. Magnetic Resonance In Medicine. Aug; 2014 72(2):563–9. [PubMed: 24006172]

20. Lu K, Liu T. Optimal phase difference reconstruction: comparison of two methods. Magnetic Resonance Imaging. 2008; 26(1):142–145. [PubMed: 17572035]

21. Hammond KE, Lupo JM, Xu D, Metcalf M, Kelley DAC, Pelletier D, et al. Development of a robust method for generating 7.0 T multichannel phase images of the brain with application to normal volunteers and patients with neurological diseases. NeuroImage. Feb; 2008 39(4):1682–1692. [PubMed: 18096412]

22. Haacke, M.; Brown, R.; Thompson, M.; Venkatesan, R. Magnetic resonance imaging: physical principles and sequence design. Wiley-Liss; 1999.

23. Kay, S. Fundamentals of Statistical Signal Processing: Estimation Theory. Prentice Hall; 1993.

24. Barrett, HH.; Myers, KJ. Foundations of Image Science. Wiley-Interscience; 2003.

25. Guerquin-Kern M, Lejeune L, Pruessmann KP, Unser M. Realistic Analytical Phantoms for Parallel Magnetic Resonance Imaging. IEEE Transactions on Medical Imaging. Mar; 2012 31(3): 626–636. [PubMed: 22049364]

26. McPhee KC, Denk C, Al Rekabi Z, Rauscher A. Bilateral filtering of magnetic resonance phase images. Magnetic Resonance Imaging. Sep; 2011 29(7):1023–1029. [PubMed: 21664782]

27. Hagmann W, Habermann J. On the phase error distribution of an open loop phase estimator. IEEE International Conference on Communications. 1988; 2:1031–1037.
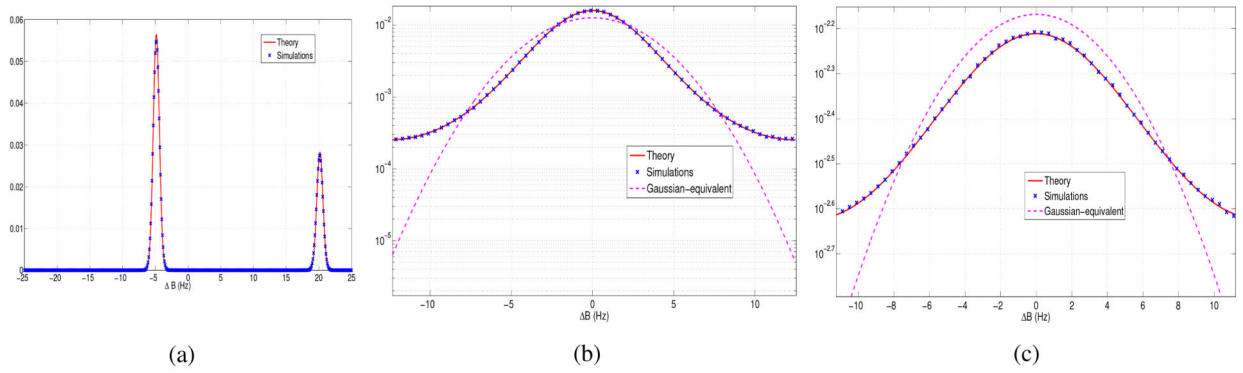
(a)  (b)  (c)

**Figure 1.**
(a)-(c) Comparison between theoretical derivations (red solid line) and numerical simulations (blue dots) in various example voxels. In (a), the maximum wrapping integer $R_{max} = 1$ and the true $B = -5$Hz. In (b) and (c) $B = 0$Hz, and $R_{max} = 0$, thus the likelihood is simply the noise distribution. The dashed magenta line is a Gaussian distribution with the same mean and standard deviation as the true noise distribution. Note the divergence between the noise probability distribution and the Gaussian approximation.

(a)



(b)
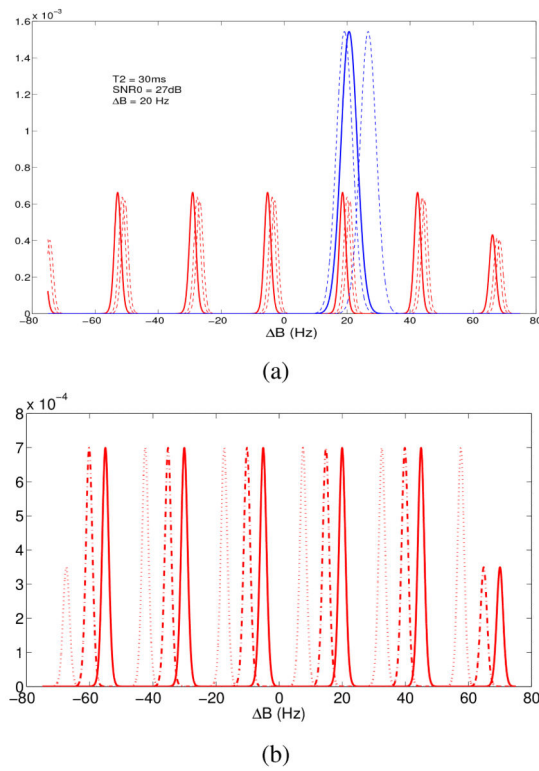
**Figure 2.**
(a) Example likelihood functions, with $\theta_{0,c} = 0$, in a voxel where $B = 20$Hz, SNR0=22 (27dB) and T2*=30ms. The family of blue lines correspond to $\mathscr{L}_{k,c}(\Delta B)$ for different $\psi_{k,c}$ realizations, at TE = 5ms. The red lines are $\mathscr{L}_{k,c}(\Delta B)$ obtained at TE = 40ms. (b) The effect of phase-offsets on $\mathscr{L}_{k,c}(\Delta B)$ is shown here for the same voxel as (a) at TE=40ms. Note that different channels will possess substantially shifted $\mathscr{L}_{k,c}(\Delta B)$ depending on their respective $\phi_{0,c}$.
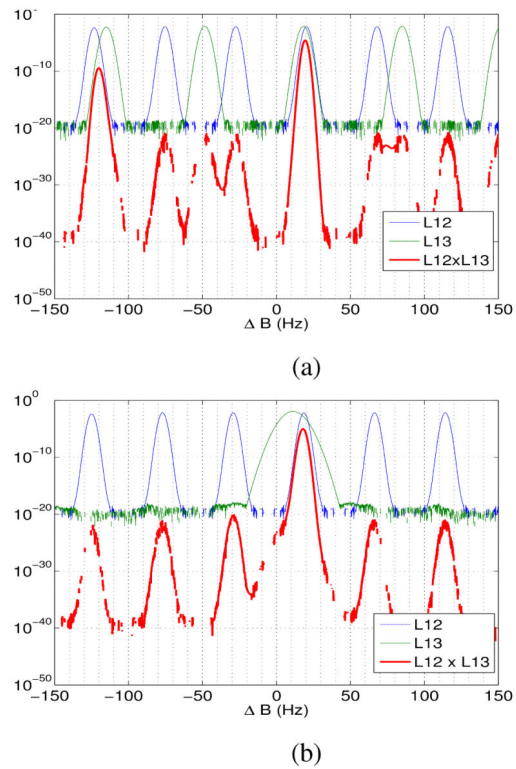
(a)



(b)

**Figure 3.**
Example system likelihood functions obtained from individual dual-echo likelihoods. Note that the system likelihoods (red) are not subject to the same noise-phase wrapping trade offs as the dual-echo likelihoods (green and blue). That is, system likelihoods do *not* always possess multiple maxima whenever the function is multimodal.
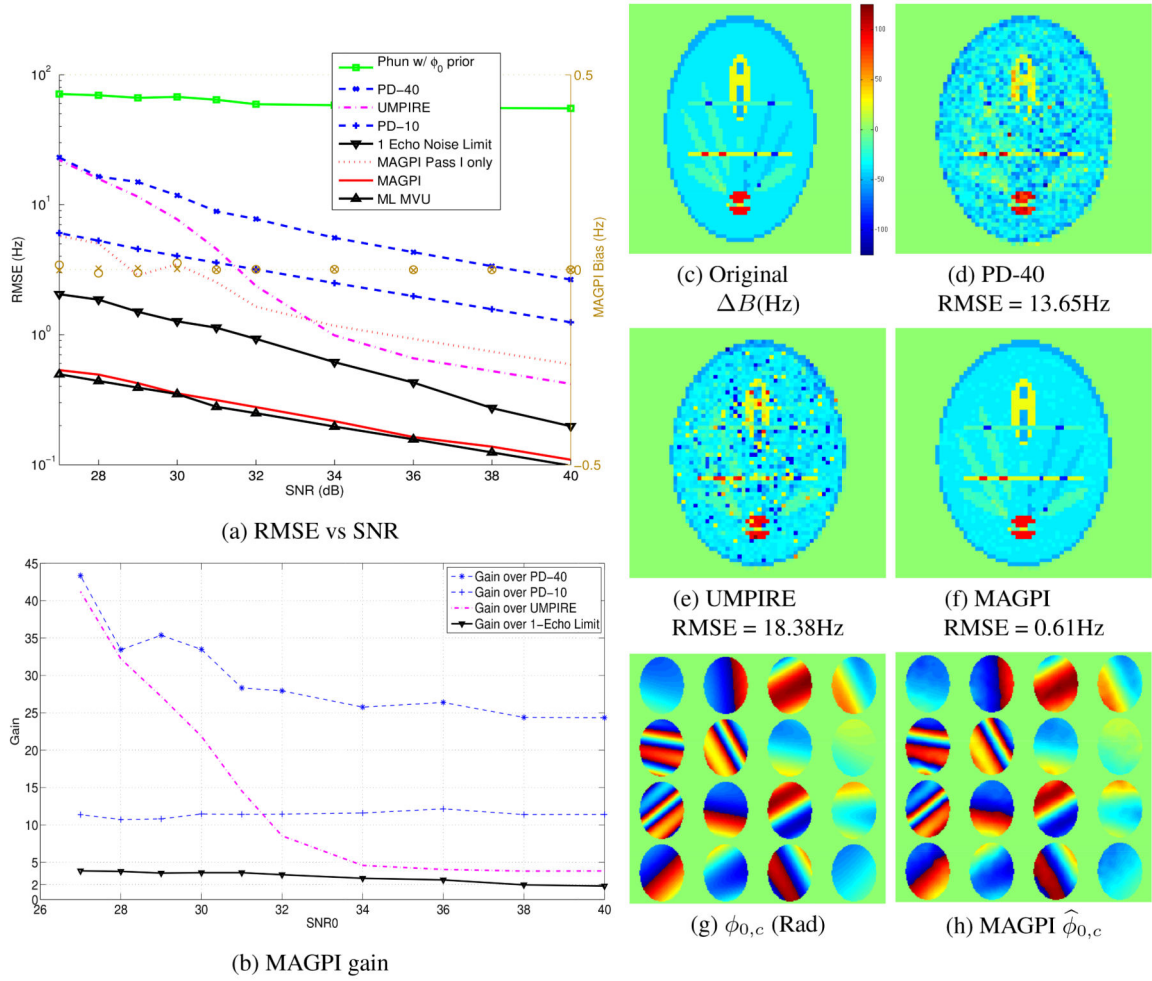
(c) Original
$\Delta B$(Hz)

(d) PD-40
RMSE = 13.65Hz

(e) UMPIRE
RMSE = 18.38Hz

(f) MAGPI
RMSE = 0.61Hz

(g) $\phi_{0,c}$ (Rad)

(h) MAGPI $\widehat{\phi}_{0,c}$

(a) RMSE vs SNR

(b) MAGPI gain

**Figure 4.**

(a) Result of Monte-Carlo simulations showing RMSE (log-scale on left) of various $B$ estimates averaged over random realizations of noise, $B$ and $\phi_{0,c}$. The bias in the MAGPI ML estimates is shown on the right axis of the plot using the o (Pass I) and × (Pass III) markers. The MVU bound (black line with triangles) and the unbiased results show that MAGPI is an efficient estimator. (b) Average RMSE reduction (or performance gain) achieved with MAGPI over select methods: at the lowest SNR of 27dB, MAGPI reduces the RMSE by 41× compared to UMPIRE, 11× compared to PD-10 and 3.9× compared the "ideal" single-echo method. We show example original tissue frequency $B$ in (c) and corresponding phase-offsets in (g). Example $B$ estimates obtained at $SNR_0$ of 27dB (or $SNR_{(TE=40ms)}$ = 8.23) using: (d) PD-40 (RMSE = 13.65Hz), (e) UMPIRE (RMSE = 18.38Hz) and (f) MAGPI (RMSE = 0.61Hz). MAGPI also generates an estimate of $\phi_{0,c}$ in (h). Phase-offsets are shown as $\angle\{\exp(i\phi_{0,c})\}$ between $[-\pi, \pi]$.
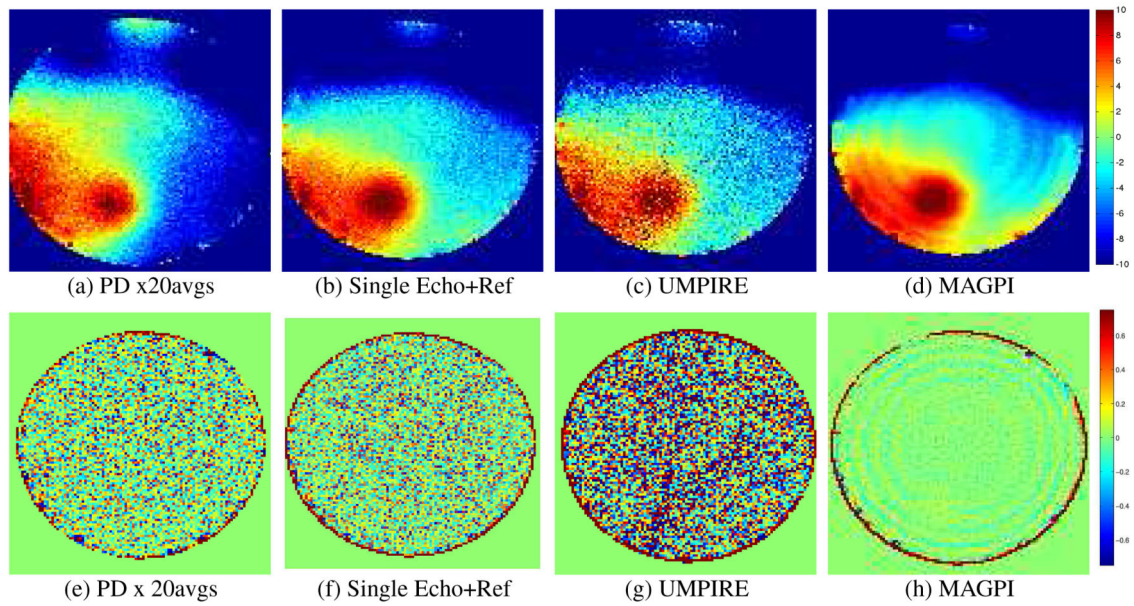
(a) PD x20avgs          (b) Single Echo+Ref          (c) UMPIRE          (d) MAGPI

(e) PD x 20avgs          (f) Single Echo+Ref          (g) UMPIRE          (h) MAGPI

**Figure 5.**
Estimated $B$ in a water phantom using (a,e) PD-10, with 20 averages, (b,f) a single echo method which uses PD-10 scan as a $\phi_{0,c}$ reference scan, (c,g) UMPIRE and (d,h) MAGPI. Bottom row is the remainder after applying background phase removal on images of top row and thus, is a measure of noise content in estimate. All units are in Hz. The reduction in noise standard deviation obtained with MAGPI was a factor of **3.95×** over PD-10 ×20avgs, **3.661×** over Single-Echo+Ref, and **7.9×** over UMPIRE. The ring patterns detected with MAGPI in (h) are also present in the magnitude image of Figure 6a. We elaborate on this observation in the Discussion section.
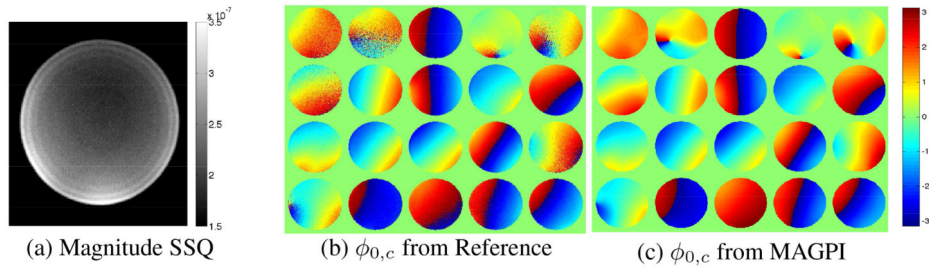
(a) Magnitude SSQ    (b) $\phi_{0,c}$ from Reference    (c) $\phi_{0,c}$ from MAGPI

**Figure 6.**
(a) The magnitude image at an early echo of 3.5ms reconstructed using standard Sum of Squares method. The phase-offset in the water phantom as estimated using (b) the PD-10 ×20 averages scan and (c) MAGPI. Note the similarity between the two estimates.
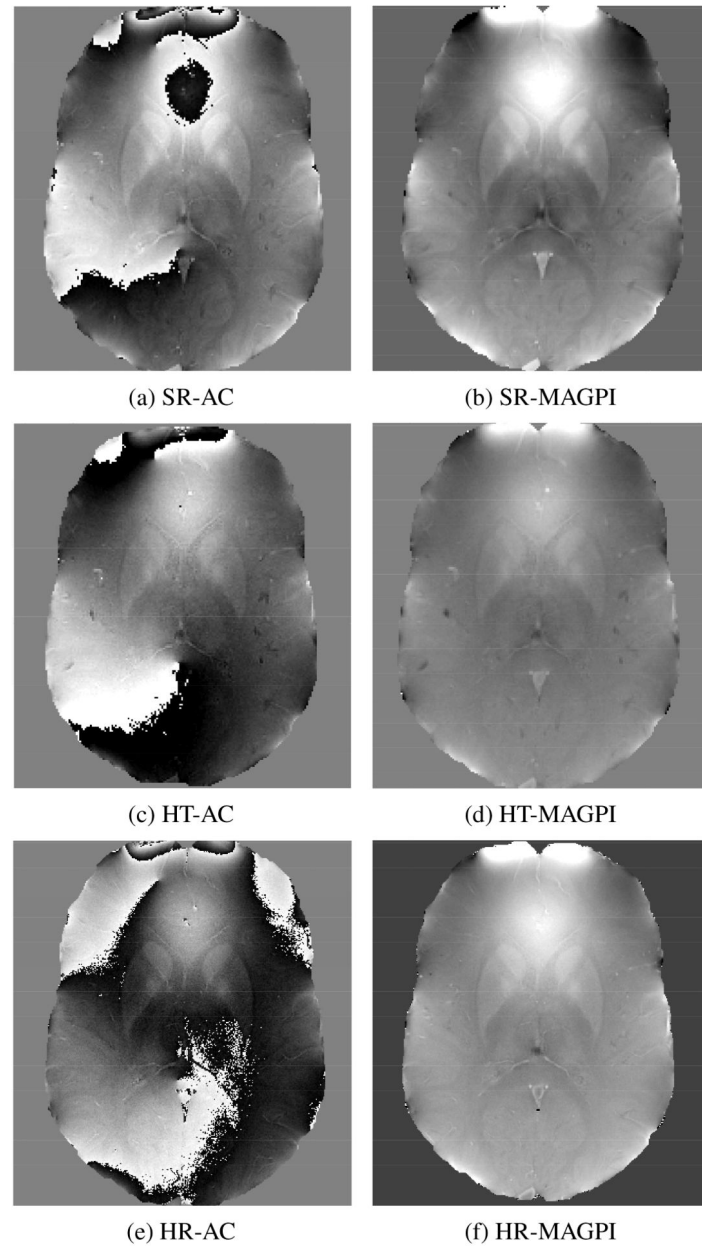
(a) SR-AC        (b) SR-MAGPI

(c) HT-AC        (d) HT-MAGPI

(e) HR-AC        (f) HR-MAGPI

**Figure 7.**
*In-vivo* $B$ maps at 1.5T, at in-plane resolution of $0.49 \times 0.49 \text{mm}^2$, obtained with (first column) traditional single echo methods with Adaptive Combine and (second column) MAGPI. Rows 1-3 represent Scans SR (Standard Resolution), HT (same as HR with half the TR) and HR (half the voxel size of SR), respectively. Note the wrapping artifacts and phase-offset inversion errors obtained with Adaptive Combine. The MAGPI $B$ estimates are obtained voxel-per-voxel, without any smoothing or phase unwrapping.

(a) SR-1Echo	(b) SR-MAGPI	(c) SR-MAGPI-BiL

(d) HT-1Echo	(e) HT-MAGPI	(f) HT-MAGPI-BiL
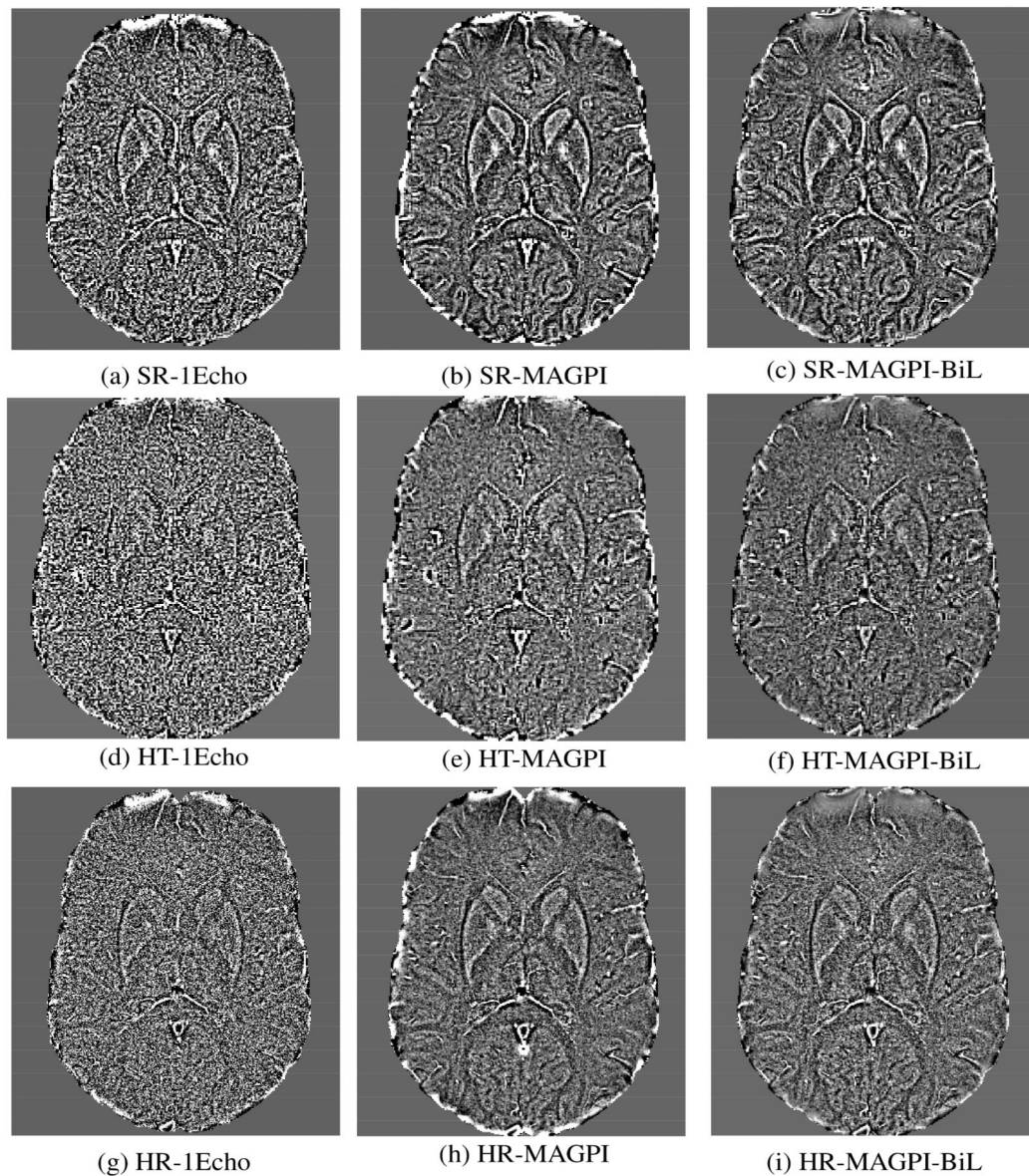
(g) HR-1Echo	(h) HR-MAGPI	(i) HR-MAGPI-BiL

**Figure 8.**
(First column) Multi-coil data from first column of Figure 7 now combined using Homodyne filtering, for each of Scans SR, HT and HR across rows. (Second column) MAGPI *B* estimates from second column of Figure 7 filtered using the same homodyne operator as the traditional method. (Third column) Same as second column, except we used a Bilateral filter instead of the traditional homodyne high pass filter. We note the following: in Scan SR, the phase SNR gain with MAGPI allows for improved resolution of fine cortical structures and basal ganglia. In Scans HT and HR, MAGPI achieves clear SNR and CNR gains over the non-diagnostic Figures 8d and 8g. Despite the challenging magnitude-domain SNR of Scans HT and HR, MAGPI still allows for improved visualization of deep brain structures with fine delineation of basal ganglia and clear distinction of caudate head and lentiform nuclei from anterior and posterior limb of internal capsule (Figures 8e,f and 8h,i).

MAGPI+bilateral filter attains improved SNR and CNR gains, without blooming artifacts, compared to MAGPI+homodyne filters (Figures 8f,i vs 8e,h). Phase images are scaled here between ±0.5Hz for Scan SR and ±1Hz for Scans HT and HR.

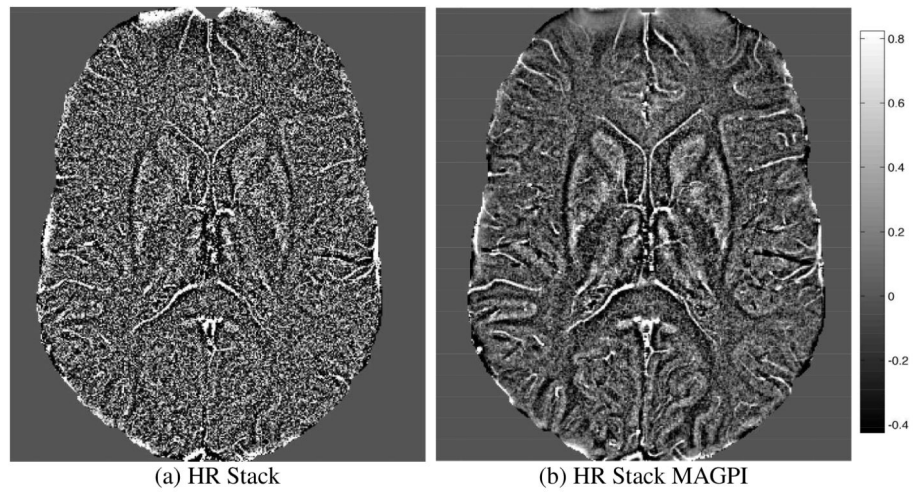(a) HR Stack                                    (b) HR Stack MAGPI

**Figure 9.**
High-pass filtered ΔB maps from Scan HR, shown across a slab of 4 slices (8mm thick) for (a) single-echo Homodyne-Processed Phase and (b) Bilateral filtered MAGPI. MAGPI enables very high resolution images at 1.5T compared to the standard method, where accentuated noise clearly impairs definition of fine structural details. The phase CNR and SNR achieved with MAGPI significantly improves the image quality, with excellent white-gray matter differentiation and clear distinction of deep brain structures such as basal ganglia.

**Table 1**

**In-Vivo Scans**

| Scan Type | Single-Echo | MAGPI | Parameters |
|-----------|-------------|-------|------------|
| Scan SR | TE = 40ms, TR = 46ms, TA = 3min30s | TE = {26.56, 35, 40.91}ms, TR = 46ms, TA = 3min40s | 3D GRE, FOV = 220(r.o.)× 200mm$^2$, $N_x$ = 256, $N_y$ = 232, $z$= 2mm, TR = 45ms, FA = 15°, BW= 240Hz/pxl, Voxel size: $0.9 \times 0.9 \times 2$ mm$^3$, $C_{TE}$: $TE_{min}$ = 6.1ms, $TE_{min}$ = 5.82ms. |
| Scan HT | TE = 20ms, TR = 23ms, TA = 1min40s | TE = {6.73, 14.63, 20.75}ms, TR = 24ms, TA = 1min40s | Same as the SR scan, except with half the TR: TR=23ms. |
| Scan HR | TE = 40ms, TR = 46ms, TA = 6min07s. | TE = {16.18, 27.98, 35.57}ms, TR = 40ms, TA = 5min20s | Same as the SR scan, except with: $N_x$ = 448, $N_y$ = 406, voxel size of $0.49 \times 0.49 \times 2$ mm$^3$; $C_{TE}$: $TE_{min}$ = 7.52ms, $TE_{min}$ = 7.00ms. |